

Manuscript number DOI:10.1002/ppap.

**Article type: Full Paper**

## **Turbulence and entrainment in an atmospheric pressure dielectric barrier plasma jet.**

Y. Morabit<sup>1</sup>, R. D. Whalley<sup>2</sup>, E. Robert<sup>3</sup>, M. I. Hasan<sup>1</sup> & J. L. Walsh<sup>1\*</sup>

<sup>1</sup>Centre for Plasma Microbiology, Department of Electrical Engineering & Electronics, University of Liverpool, L69 3GJ, UK.

<sup>2</sup>School of Mechanical and Systems Engineering, Newcastle University, NE1 7RU, UK.

<sup>3</sup>GREMI UMR 7344 CNRS/Université d'Orléans, Orléans, 45067, France.

### **Abstract**

Particle Image Velocimetry, Laser-Induced Fluorescence, and computational modeling are used to quantify the impact of plasma generation on air entrainment into a helium plasma jet. It is demonstrated that discharge generation yields a minor increase in the exit velocity of the gas. In contrast, the laminar to turbulent transition point is strongly affected, attributed to an increase in plasma-induced perturbations within the jet shear layer. The temporal decay of laser-induced fluorescence from OH is used as an indicator for humid air within the plasma. The results show that plasma-induced perturbations increase the quenching rate of the OH fluorescent state; indicating shear layer instabilities play a major role in determining the physicochemical characteristics of the plasma.

\*Corresponding author: [jlwalsh@liverpool.ac.uk](mailto:jlwalsh@liverpool.ac.uk)

# 1     **1     Introduction**

2     Atmospheric pressure plasma jets have been widely used in many healthcare and materials  
3     processing applications, ranging from etching and deposition to microbial decontamination and  
4     cancer therapy.<sup>[1-5]</sup> Perhaps the most widely used plasma jet configuration is based on the dielectric  
5     barrier discharge employing a noble gas such as helium or argon; typically, the gas is flushed  
6     through a dielectric capillary and subjected to an applied voltage using one or more electrodes  
7     placed inside and/or outside of the capillary. On application of a time-varying voltage of sufficient  
8     magnitude to cause breakdown, a discharge forms within the capillary and propagates as a fast-  
9     moving ionization wave along the noble gas channel, ultimately exiting the capillary and extending  
10    into the surrounding quiescent air. From an application perspective, atmospheric pressure plasma-  
11    based applications typically rely on reactive oxygen and nitrogen species (RONS), many of which  
12    are created through the interaction between the plasma plume and the quiescent air.

13  
14    A large number of studies have considered the impact that plasma generation has on the  
15    characteristics of the flowing noble gas. It has been widely reported that the generation of plasma in  
16    a buoyant axisymmetric jet configuration leads to a rapid transition from laminar to turbulent  
17    flow.<sup>[6-10]</sup> It is commonly assumed that gas heating and Electrohydrodynamic (EHD) forces play a  
18    role in creating turbulence within the flowing gas channel, with the latter being considered as the  
19    dominant mechanism. Indeed, Park et al. used a pulsed plasma jet to demonstrate that EHD forces  
20    are primarily exerted by space charge drifting in the applied electric field following streamer  
21    propagation, confirming the modelling results of Hasan and colleagues.<sup>[11, 12]</sup> Whalley and Walsh  
22    demonstrated that the spatially developing velocity fields in an inhomogeneous axisymmetric  
23    plasma jet flow are turbulent and self-similar, with characteristics matching the turbulent velocity  
24    fields which develop naturally with increasing distance from the jet exit. Using an order-of-  
25    magnitude analysis, it was predicted that the presence of a discharge should only increase the jet  
26    exit velocity by approximately 10%.<sup>[8]</sup> Many works in the field of fluid dynamics have indicated

27 that the generation of turbulence in an axisymmetric jet flow is related to small-amplitude body  
28 forces causing perturbations in the unstable shear layers at the jet exit, which grow as they move  
29 downstream.<sup>[13-17]</sup>

30  
31 To characterize the chemical species produced downstream of the jet orifice, multiple invasive and  
32 non-invasive diagnostic techniques have been applied, including tuneable diode laser absorption  
33 spectroscopy (TDLAS),<sup>[18]</sup> mass spectroscopy (MS),<sup>[19]</sup> Fourier transform infrared spectroscopy  
34 (FTIR),<sup>[16]</sup> Laser-Induced Fluorescence (LIF) and Two-photon Absorption Laser-Induced  
35 Fluorescence (TALIF).<sup>[21-23]</sup> Of all the techniques investigated, LIF based methods are particularly  
36 convenient as they provide the high spatiotemporal resolution required to accurately investigate the  
37 complex downstream chemistry in a plasma jet while facilitating the quantification of absolute  
38 radical densities. Regardless of the diagnostic technique used, it is clear that a significant proportion  
39 of the reactive chemical species produced within the downstream region of the jet are a result of  
40 reactions between the noble gas plasma and molecular gas impurities entrained from the  
41 surrounding environment, which is typically humid air. Given that the interplay between the  
42 propagating plasma plume and ambient environment has a considerable impact on the  
43 physicochemical properties of the plasma jet and, therefore, on the application efficacy,  
44 understanding the underpinning mechanisms of how air becomes entrained within the flowing noble  
45 gas channel is of vital importance.

46  
47 This study investigates the entrainment of air into a helium plasma jet and explores the hypothesis  
48 that small perturbations within the jet shear layer resulting from plasma generation not only result in  
49 the early onset of turbulence but also act to increase entrainment of air into the laminar region of the  
50 jet. Particle image velocimetry (PIV) was used to quantify the fluid dynamics of the helium jet flow  
51 beyond the jet orifice and combined with LIF to provide a sensitive means of assessing the  
52 entrainment of humid air into the discharge.

53

## 54 **2 Experimental and computational methods**

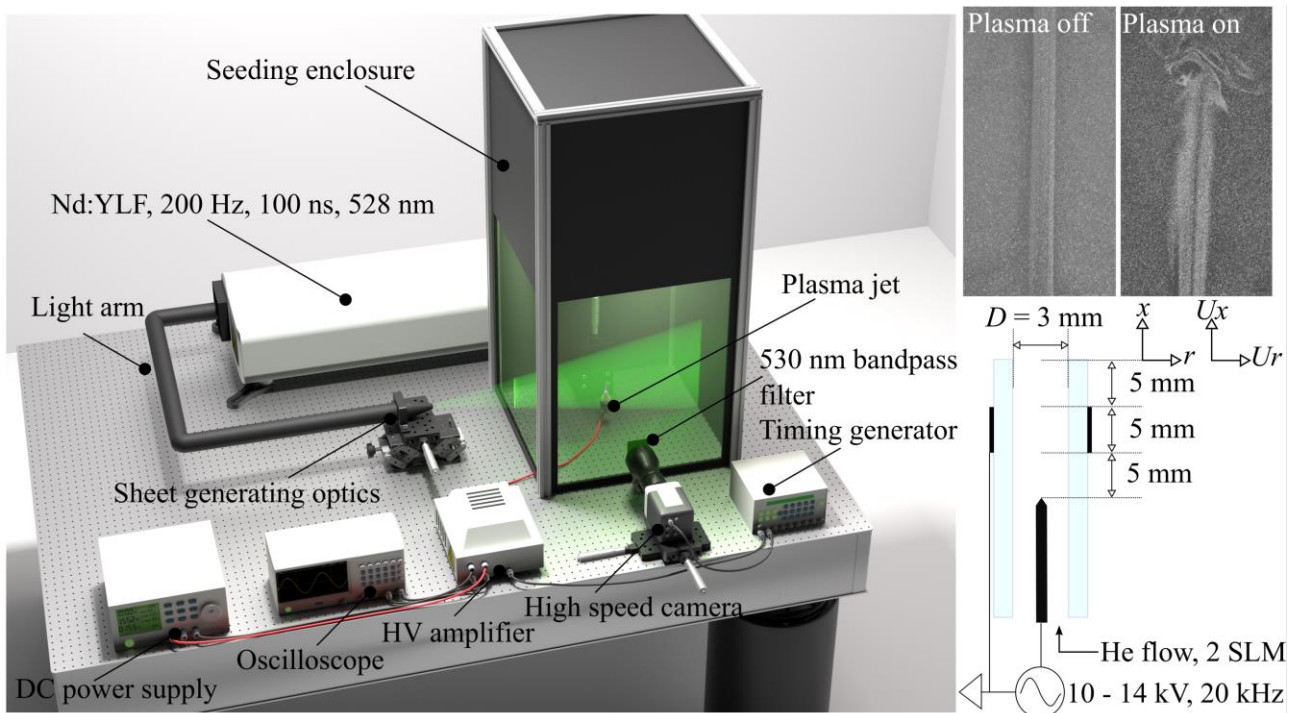
### 55 **2.1 Plasma Jet and PIV setup**

56 The plasma jet used in this study comprised of a quartz capillary with an inner diameter  $D$ , equal to  
57 3 mm and an outer diameter of 5 mm, a metallic strip was wrapped around the outer diameter of the  
58 capillary to act as a ground electrode, as shown in **Figure 1**. A tungsten pin was positioned  
59 coaxially within the quartz capillary and connected to a high-voltage sinusoidal power source  
60 operating at a frequency of 20 kHz. Two applied voltage cases were examined in this study, 14  
61 kVpp and 10 kVpp, with the latter being just above the point of gas breakdown. Helium gas with a  
62 purity of 99.999% was flushed through the capillary at 2 Standard Liters per Minute (SLM), giving  
63 a maximum exit velocity,  $U_m$ , equal to  $9.4 \text{ m s}^{-1}$ .

64

65 To quantify the flow field created by the plasma jet, PIV measurements were undertaken using the  
66 experimental setup shown in Figure 1. The plasma jet was inserted into a large sealed chamber  
67 (volume  $> 2 \text{ m}^3$ ), which was seeded using oil droplets with a nominal size of  $1 \mu\text{m}$ . The chamber  
68 ensured that the plasma jet flow was not influenced by any external draughts. A similar  
69 experimental arrangement was used in the previous works of the authors,<sup>[8]</sup> where it was observed  
70 that an insufficient number of seeding particles were entrained within the laminar region of the jet  
71 to obtain reliable PIV measurements. To overcome this challenge, the helium flow into the jet  
72 capillary was seeded using oil droplets, which also had a nominal size of  $1 \mu\text{m}$ . The addition of oil  
73 droplets to the helium gas flow has an obvious potential to disrupt the discharge; while such  
74 changes are difficult to assess, the breakdown voltage and length of plasma plume were found not  
75 to change significantly. Furthermore, Rayleigh scattering was used to obtain an approximate  
76 indication of the laminar region length in an un-seeded jet and a close agreement was observed  
77 when compared to the PIV measurements on the seeded jet, suggesting the presence of the seeding  
78 particles had a minimal impact on the fluid dynamic properties of the system. Given the nominal

79 size of the seeding particles, the Stokes number was found to be less than 0.1, thus ensuring that the  
 80 particles followed the fluid flow closely with tracing errors being  $< 1\%$ .<sup>[24]</sup>  
 81  
 82 Planar velocity measurements were conducted using a 2D particle image velocimetry system from  
 83 TSI inc. The system consisted of a double pulsed Nd:YLF laser operating at 200 Hz with a pulse  
 84 duration of 100 ns at a wavelength of 527 nm and was used to generate a 1 mm thick light sheet that  
 85 was projected into the seeding chamber and across the plasma jet orifice. A high-speed Phantom  
 86 Miro Lab 340 camera was positioned outside the seeding chamber normal to the laser sheet and  
 87 synchronized with the laser such that each frame captured a single laser pulse. A spatial calibration  
 88 was performed and the time delay between consecutive laser pulses ( $\Delta t$ ) was set to 30  $\mu\text{s}$ , a value  
 89 chosen to capture the movement of oil droplets over a grid with spatial dimensions of 350  $\mu\text{m}^2$ ,  
 90 enabling the velocity vectors to be computed using a recursive cross-correlation technique. For each  
 91 measurement condition, the plasma jet was operated for several seconds before data capture to  
 92 ensure steady-state conditions were achieved. Each dataset comprised of 800 frames that were used  
 93 to make 400 individual velocity vector maps; in the case of time-averaged measurements, all 400  
 94 vector maps were averaged and presented as a single figure.



96 **Figure 1.** Diagram showing the layout of the particle image velocimetry experiment and  
97 configuration of the plasma jet device, with representative PIV images for the plasma off and  
98 plasma on cases, vectors  $U_x$  and  $U_r$  represent the axial and radial velocity components, respectively.  
99

## 100 2.2 LIF setup and OH density calibration

101 The LIF measurement system used in the investigation is shown in **Figure 2**, the system was used  
102 to measure OH radical density and to obtain an indication of air entrainment within the plasma  
103 plume through the measurement of the radiative decay time of the laser-excited OH(A) state. The  
104 system comprised of a tuneable dye laser (Sirah Cobra Stretch with second harmonic generation  
105 unit) pumped by a 6 ns pulsed Nd:YAG laser with a wavelength of 532 nm, pulse energy of 120 mJ  
106 and a repetition rate of 10 Hz. A number of LIF excitation schemes have been proposed for the  
107 measurement of OH radicals in atmospheric pressure plasmas.<sup>[25-27]</sup> In this work, the dye laser was  
108 tuned to generate an output at a wavelength 282.58 nm to excite the P<sub>1</sub>(2) transition from the  $f_1(2)$   
109 rotational level of OH X( $v'' = 0$ ) to the F<sub>1</sub>(1) rotational level of OH A( $v' = 1$ ). A number of  
110 previous studies have used a similar excitation scheme due to the P<sub>1</sub>(2) transition being spectrally  
111 separated from adjacent lines and the  $f_1(2)$  level having the largest relative population in the  
112 temperature range under investigation.<sup>[28]</sup>

113  
114 The 282.58 nm beam emitted from the dye laser was measured to have a pulse energy in excess of  
115 17 mJ, a value several orders of magnitude above the range linear LIF measurements are typically  
116 made (1 – 10  $\mu$ J).<sup>[29]</sup> Operation beyond the linear region greatly complicates the interpretation of the  
117 results, as the ground rotational level is significantly depleted by light absorption and partially  
118 refilled by fast rotational redistribution, altering the LIF outcome dependent on the unknown gas  
119 composition and temperature. To attenuate the laser energy to a suitable range an optical  
120 arrangement similar to that employed by Ries et al. was adopted,<sup>[21]</sup> two quartz plates were angled  
121 to split the beam as shown in Figure 2, with a small fraction being reflected towards the plasma jet

122 and the majority of the beam passing through to beam dumps mounted behind each plate. Following  
123 attenuation, the beam was directed through an uncoated quartz plano-convex lens with a focal  
124 length of 1 m, and a pinhole of 1 mm was positioned to act as a spatial filter, further attenuating the  
125 beam. Using this approach, the maximum laser pulse energy was found to be approximately 15  $\mu\text{J}$ ;  
126 small changes to the Q-switch delay of the pump laser were subsequently used to vary the pulse  
127 energy between 1 and 15  $\mu\text{J}$ . Laser power was measured using a Thorlabs PM100D optical power  
128 and energy meter equipped with a thermal volume absorber power sensor.

129

130 To capture the fluorescence of excited OH molecules, an Andor iStar740 iCCD camera was fitted  
131 with a Jenoptik UV 105 mm f/4.5 imaging lens. The camera arrangement was positioned to face the  
132 plasma jet perpendicular to the laser beam. For each image recorded, the iCCD camera was  
133 configured to accumulatively capture 500 laser pulses, using an optical gate width equal to 8 ns for  
134 each exposure. Following the approach of Verreycken et al.,<sup>[28]</sup> no bandpass filter was used during  
135 LIF measurements to avoid the need for additional corrections in the calibration procedure. A  
136 consequence of this approach is the potential for interference of the fluorescent signal from other  
137 emissions within the plasma and the Rayleigh scattering signal. A background subtraction of the  
138 emission captured with the plasma energized and laser de-tuned was used to correct for light  
139 emitted by the plasma and any scattered light. To ensure the measurements were conducted within  
140 the linear LIF region, the measured LIF intensity was plotted against laser energy and a linear fit  
141 applied. It was determined that the linear range was between 1  $\mu\text{J}$  to 10  $\mu\text{J}$ , a value in close  
142 agreement with several past LIF investigations.<sup>[21, 28]</sup>

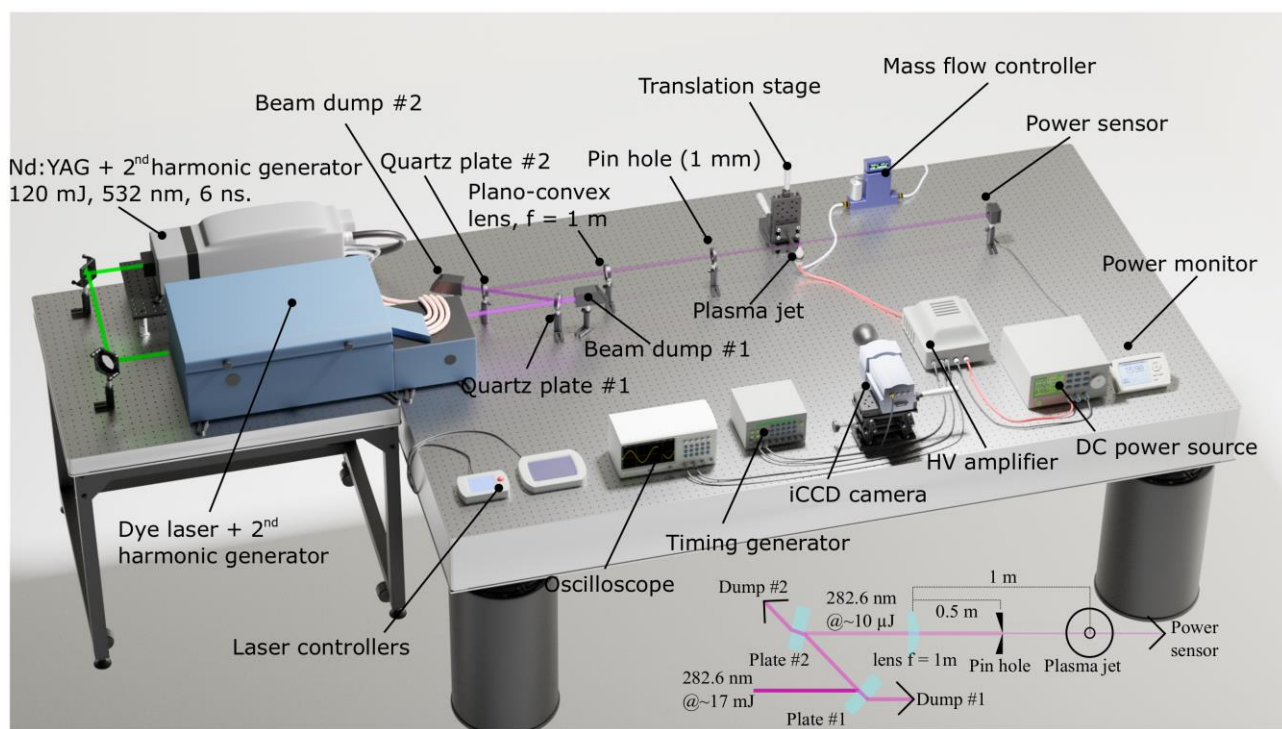


**Figure 2.** Diagram showing the layout of the Laser-Induced Fluorescence experiment, insert highlights optical arrangement used to achieve a three-order reduction in laser intensity.

143

144

145

146

147

148

149

150

151

152

153

154

155

156

157

158

159

Absolute calibration of the LIF signal to determine the density of ground-state OH can be achieved via several methods, including UV absorption, chemical modeling, and Rayleigh scattering.<sup>[28, 30]</sup> In this investigation, the Rayleigh scattering approach was adopted due to its high degree of accuracy, and a similar methodology to that described by Verreycken et al. was adopted.<sup>[28]</sup> Calibration by Rayleigh scattering requires detailed knowledge of the rotational and vibrational energy transfer rates, which vary significantly depending on the nature of the quenchers present; thus an accurate appreciation of the gas composition is essential. Careful consideration must be applied in the case of a plasma jet as the gas composition varies as a function of distance from the jet orifice; further details on this are provided in section 2.3. Also important for the determination of absolute OH density is the decay time of the laser-excited fluorescent state. This was measured at each spatial position by applying a time delay to the iCCD camera from 6 ns (*i.e.*, immediately after the laser pulse) up to 2000 ns; at each time point the fluorescent intensity from 500 laser shots was accumulated to form a single image. From each image, the sum of LIF intensity in a  $0.36 \text{ mm}^2$



160 interrogation area on the jet centreline was determined and plotted as a function of delay time, an  
 161 exponential fit was applied to determine the decay rate at each spatial position.

162 In addition to the gas composition, the gas temperature can also affect the interpretation of the LIF  
 163 data. To investigate the influence of plasma generation on gas temperature, an Omega FOB100  
 164 fiber-optic thermometer was used, the dielectric temperature probe was positioned in the plasma at  
 165 various points downstream of the jet orifice and the temperature recorded. The temperature was  
 166 found to vary little with spatial position, with a maximum of 10 K above ambient located close to  
 167 the capillary orifice, such observations are in-line with previous studies.<sup>[8]</sup>

168 The remainder of the calibration process closely followed that reported previously by Verreycken et  
 169 al. and will only be summarized in brief here.<sup>[28]</sup> To obtain Rayleigh scattering data for calibration,  
 170 the jet capillary was supplied with Nitrogen gas at a flow rate of 2 SLM, while not strictly  
 171 necessary, the nitrogen flow helped to ensure dust from the ambient environment did not enter the  
 172 measurement region of interest. The laser power was varied from 2 to 15  $\mu\text{J}$  in 1  $\mu\text{J}$  increments, and  
 173 the sum of the Rayleigh scattered signal intensity in a square region of interest measuring 0.36  $\text{mm}^2$   
 174 was calculated. The measured Rayleigh scattered signal,  $S_{Ray}$  (#counts), can be written as:

$$S_{Ray} = \eta N_n \frac{\partial^{\beta=0} \sigma_0}{\partial \Omega} V_{Ray} I_L t_L \quad (1)$$

178 Where  $\eta$  is the calibration constant (#counts sr  $\text{J}^{-1}$ ),  $N_n$  is the density of scattering particles ( $\text{m}^{-3}$ ),  
 179  $\partial^{\beta=0} \sigma_0 / \partial \Omega$  is the differential cross-section for Rayleigh scattering ( $\text{m}^2 \text{sr}^{-1}$ ),  $V_{Ray}$  is the volume from  
 180 which Rayleigh scattering is collected ( $\text{m}^3$ ),  $I_L$  is the laser irradiance ( $\text{W m}^{-2}$ ) and  $t_L$  is the temporal  
 181 length of the laser pulse (s), which was measured by replacing the power meter shown in Figure 2  
 182 with a fast photodetector. After considering the non-uniformity of the laser energy density,  
 183 Equation (1) becomes:

$$S_{Ray} = \eta N_n \frac{\partial^{\beta=0} \sigma_0}{\partial \Omega} E_L \Delta x \quad (2)$$

186

187 Where  $E_L$  is the laser energy (J), and  $\Delta x$  is the length of the detection volume (m). Following this,  
188 the calibration constant  $\eta$  was obtained from the slope  $\alpha$ , of the measured Rayleigh intensity as a  
189 function of laser energy multiplied by pressure:

190

$$191 \quad \eta = \alpha k_B T \frac{\partial^{\beta=0} \sigma_0}{\partial \Omega} \Delta x \quad (3)$$

192

193 Where  $k_B$  is the Boltzmann constant and  $T$  is the temperature (K). Using the calibration factor, the  
194 intensity of the laser-induced fluorescence  $S_{LIF}$ , can be expressed as:

195

$$196 \quad S_{LIF} = \frac{1}{4\pi} \int \eta E n_{exc}(x, y, z, t) A \, dx dy dz dt \quad (4)$$

197

198 Where  $E$  is the energy gap according to the chosen transition,  $A$  is the Einstein emission coefficient  
199 ( $s^{-1}$ ), and  $n_{exc}(x, y, z, t)$  is the density of OH in the excited state. To determine the ground state OH  
200 density based on  $n_{exc}$  in Equation (4), the 4-level collisional radiative model reported by Verreycken  
201 et al. was utilized.<sup>[28]</sup> Briefly, the model follows the densities of 3 laser-excited levels of OH in  
202 addition to the ground state. The followed levels are the ground state OH X( $v''=0$ ), OH A( $v'=1$ ),  
203 OH A( $v'=0$ ), and OH X( $v''=1$ ). For each level an ordinary differential equation is solved describing  
204 the gains and the losses of that level, leading to a coupled system of 4 equations. The processes  
205 described in the system are the radiative excitation by the laser, the quenching by air constituents,  
206 and the vibrational relaxation. It is assumed in the model that the rotational energy transfer is much  
207 faster than the other processes; thus, the rotational levels are not resolved. The inputs to the 4-level  
208 model include the experimental parameters listed in **Table 1**, the gas composition determined by the  
209 flow model described in section 2.3, and an estimated ground state OH density. Solving the 4-level  
210 model provides a prediction of the LIF signal intensity, which by comparison to the measured LIF  
211 signal intensity is used to determine the actual ground-state OH density. Full details of the

212 implementation can be found in the works of Verreycken and colleagues.<sup>[28]</sup> Finally, Table 1 shows  
 213 the relevant experimental parameters used in the LIF measurements, and these were also used as  
 214 inputs for the computational model.

215

216 *Table 1.* Experimental parameters used in LIF measurements and absolute density calibration

Parameter	Description	Value
$\lambda_L$	Laser wavelength	282.58 [nm]
$\Delta\lambda_L$	Linewidth of the laser	0.95 [pm]
$g_{int}$	Overlap integral	0.017 [m]
$A_L$	Area of the laser beam	0.0746 [mm <sup>2</sup> ]
$E_L$	Laser energy per pulse	10 [ $\mu$ J]
$\tau_L$	Temporal FWHM of the laser pulse	6 [ns]
$\Delta x$	Length of the detection volume	0.359 [mm]
$\Delta y$	Width of the detection volume	0.359 [mm]
$\Delta s$	The spatial FWHM of the laser beam at the observation point	0.1795 [mm]

217

218

### 219 **2.3 Computational model and statistical analysis methodology**

220 To account for the varying composition of gas downstream of the jet orifice, a computational model  
 221 was developed that solved for the velocity field of the gas mixture in addition to the mass fractions  
 222 of its constituents, namely N<sub>2</sub>, O<sub>2</sub>, H<sub>2</sub>O, and He. To obtain the velocity field, the model solved the  
 223 mass continuity Equation (5), which solves for the mass density of the entire gas mixture, and the  
 224 momentum conservation Equation (6). To compute the densities of the species constituting the gas  
 225 mixture, the continuity equation, given by Equation (7), was solved for the mass fraction of three  
 226 species, while the mass fraction of the fourth was determined from the pressure constraint. All  
 227 equations were solved in steady-state mode (*i.e.*, time-independent equations):

$$228 \quad \nabla \cdot (\rho \vec{u}) = 0 \quad (5)$$

$$229 \quad \rho(\vec{u} \cdot \nabla) \vec{u} = -\nabla p + \nabla \cdot \left( \mu(\nabla \vec{u} + \nabla \vec{u}^T) - \frac{2}{3} \mu(\nabla \cdot \vec{u}) I \right) - (\rho - \rho_0) g \quad (6)$$

$$230 \quad \rho(\vec{u} \cdot \nabla) \omega_i + \nabla \cdot (\vec{\Gamma}_i) = 0 \quad (7)$$

231 Where  $\rho$  is the density of the gas mixture ( $\text{kg m}^{-3}$ ),  $\vec{u}$  is the velocity field of the gas mixture ( $\text{m s}^{-1}$ ),  
 232  $p$  is the gas mixture's pressure (Pa),  $\mu$  is the gas mixture's viscosity (Pa s),  $I$  is the identity matrix,  
 233  $\rho_0$  is the density of air ( $\text{kg m}^{-3}$ ), and  $g$  is the gravitational constant ( $\text{m s}^{-2}$ ),  $\omega_i$  is the mass fraction of  
 234 the  $i^{\text{th}}$  species, and  $\Gamma_i$  is the diffusive flux of the  $i^{\text{th}}$  species, which is calculated according to  
 235 Maxwell-Stefan theory for diffusion as given by Equation (8 - 10).<sup>[31, 32]</sup>

$$236 \quad \vec{\Gamma}_i = \rho \omega_i \vec{V}_i \quad (8)$$

$$237 \quad \nabla x_i = \sum_{j=1}^4 \frac{x_i x_j}{D_{ij}} (\vec{V}_j - \vec{V}_i) + \frac{\nabla p}{p} (\omega_i - x_i) \quad (9)$$

$$238 \quad x_i = \frac{M_n}{M_i} \omega_i \quad (10)$$

239 Where  $\vec{V}_i$  is the diffusion velocity of the  $i^{\text{th}}$  species ( $\text{m s}^{-1}$ ),  $x_i$  is the mole fraction of the  $i^{\text{th}}$  species  
 240 (dimensionless), which is related to the mass fraction by Equation (8), and  $D_{ij}$  is the binary  
 241 diffusion coefficients between the  $i^{\text{th}}$  and the  $j^{\text{th}}$  species ( $\text{m}^2 \text{s}^{-1}$ ). A list of the binary diffusion  
 242 coefficients used in the model is given in **Table 2**. It should be noted that Equation (9) is  
 243 incorporated in the model as a constraint linking the flux term and the mass fraction term in  
 244 Equation (7). In Equation (10),  $M_i$  and  $M_n$  are the molecular weight of the  $i^{\text{th}}$  species and the average  
 245 molecular weight, respectively ( $\text{kg mol}^{-1}$ ). Lastly, the computational domain and the boundary  
 246 conditions used are described in the supplementary information.

247

248 *Table 2.* A list of binary diffusion coefficients used in the model.

Combination	Diffusion coefficient [ $\text{m}^2 \text{s}^{-1}$ ]	Reference
N <sub>2</sub> – He	$6.78 \times 10^{-5}$	[33]
N <sub>2</sub> – O <sub>2</sub>	$2.09 \times 10^{-5}$	[34]
N <sub>2</sub> – H <sub>2</sub> O	$2.54 \times 10^{-5}$	[35]
O <sub>2</sub> – He	$7.36 \times 10^{-5}$	[33]
He – H <sub>2</sub> O	$8.36 \times 10^{-5}$	[35]
O <sub>2</sub> – H <sub>2</sub> O	$3.185 \times 10^{-5}$	[35]

249

250 As stated in the introduction section, it is hypothesized that plasma-induced turbulence affects the  
 251 flow's velocity field and thus the gas composition. To account for such effects in the computational

252 model, the Reynolds-Averaged Navier-Stokes (RANS) approach for modeling turbulence was  
 253 followed, where a turbulent viscosity  $\mu_T$  (also known as eddy viscosity) was added to the viscosity  
 254 of the gas mixture. The eddy viscosity is a mathematical means to describe the loss of momentum  
 255 of the flow as a result of turbulence as an “effective” viscosity that is added to the physical viscosity  
 256 of the fluid. Similarly, a turbulent diffusivity  $D_T$  is added to the binary diffusion coefficients.<sup>[32]</sup> The  
 257 computation of the eddy viscosity is typically done using one of the conventional RANS turbulence  
 258 models, such as the  $k - \varepsilon$  model. Considering that such models were calibrated for flows without  
 259 plasma, their use for plasma modified flows will yield results with unknown accuracy. To overcome  
 260 this challenge, statistical analysis of the PIV data was conducted to obtain the necessary parameters  
 261 to calculate the eddy viscosity resulting from the plasma generation. Following the  $k - \varepsilon$  modeling  
 262 approach, the turbulent kinetic energy  $k$  ( $\text{m}^2 \text{s}^{-2}$ ) and the turbulent kinetic energy dissipation rate  $\varepsilon$   
 263 ( $\text{m}^2 \text{s}^{-3}$ ) are defined by Equation (11) and (12).<sup>[36]</sup>

$$264 \quad k = \frac{1}{2} \left( \overline{u'_r{}^2} + \overline{u'_x{}^2} \right) \quad (11)$$

$$265 \quad \varepsilon = 2\nu \overline{s'_{ij} \cdot s'_{ij}} \quad (12)$$

266 Where  $u'_r$  and  $u'_x$  are the time fluctuating velocity field components with respect to the average  
 267 velocity field, which were calculated from PIV data by subtracting the time-averaged velocity field  
 268 from each of the 400 instantaneous velocity maps captured during a measurement, then averaging  
 269 the square of these fluctuations. In Equation (12),  $\nu$  is the kinematic viscosity ( $\text{m}^2 \text{s}^{-1}$ ), and  $s'_{ij}$  is the  
 270 fluctuating deformation rate of the fluid ( $\text{s}^{-1}$ ), which was calculated from the PIV data as outlined by  
 271 Xu and colleagues.<sup>[37]</sup> After calculating  $k$  and  $\varepsilon$  the eddy viscosity was calculated according to  
 272 Equation (13).<sup>[36]</sup>

$$273 \quad \mu_T = \rho C \frac{k^2}{\varepsilon} \quad (13)$$

274 Where  $C$  is a constant equal to 0.0016 and  $\rho$  is the self-consistent gas mixture density calculated by  
 275 the model. The turbulent diffusivity  $D_T$  is related to the eddy viscosity by Equation (14).<sup>[28]</sup>

$$276 \quad D_T = \frac{\mu_T}{\rho S C_T} \quad (14)$$

277 Where  $Sc_T$  is the turbulent Schmidt number, obtaining an accurate value for this in a plasma-  
278 modified flow is not possible; however, the turbulent Schmidt number is close to unity for a wide  
279 variety of gas flows under very diverse conditions; hence it is assumed to be 1 in this  
280 investigation.<sup>[38]</sup> The model was subsequently solved with the experimental input of  $\mu_T$  and  $D_T$ ,  
281 which were smoothed and mirrored, then added to their physical counterpart quantities. The model  
282 was solved for both applied voltage cases investigated in this work, in addition to an unperturbed  
283 laminar case, where the eddy viscosity and diffusivity were set to zero.

284

285 As described in section 2.2, the radiative collisional model consisted of a system of Ordinary  
286 Differential Equations (ODE) describing the LIF transitions. The system was solved at every point  
287 in the computational domain close to the jet's orifice ( $x < 20$  mm,  $x/D < 7$ ), with the gas  
288 composition required for the ODEs being taken from that calculated by the fluid flow model. To  
289 quantify the density of ground-state OH, the 4-level model reported by Verreycken et al. was  
290 adopted.<sup>[28]</sup> To validate the developed computational model, the predicted LIF signal decay times  
291 were compared to those measured experimentally at multiple points along the jet axis; a close  
292 agreement was observed and is further discussed in the results section.

293

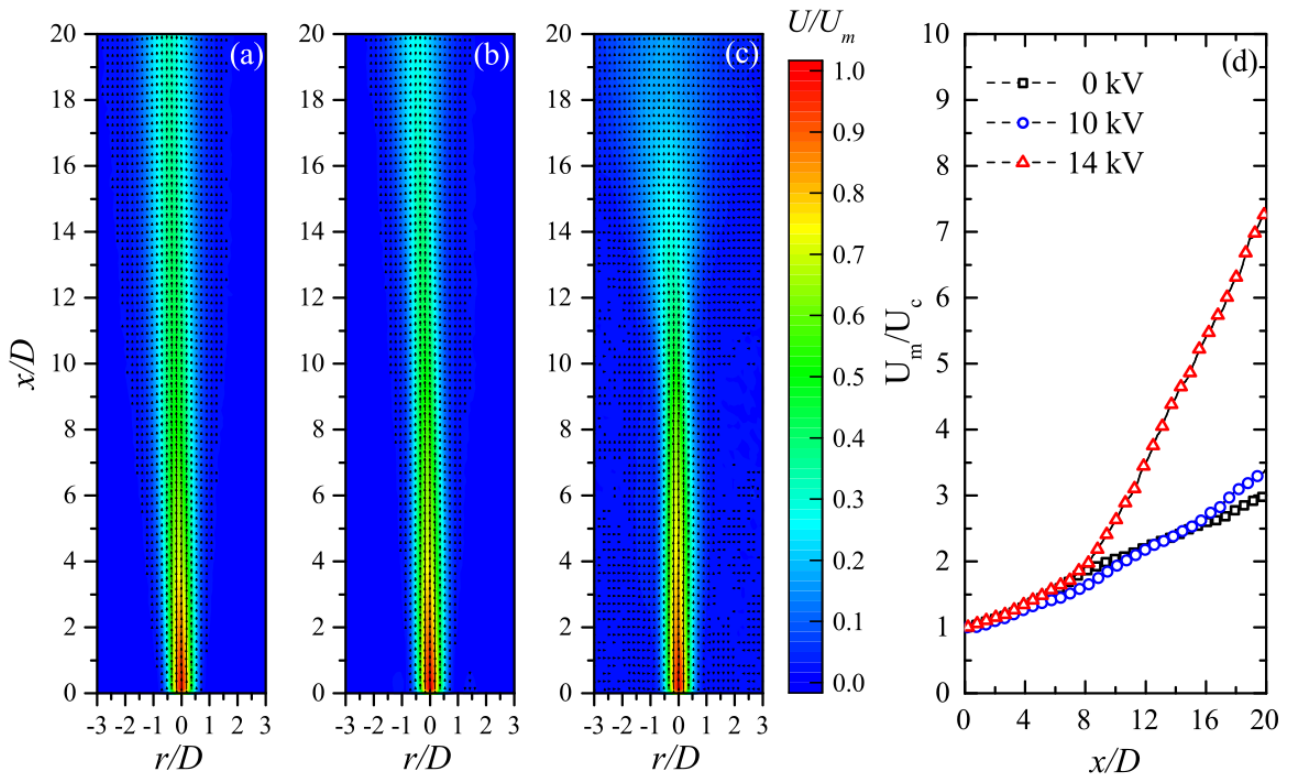
## 294 **3 Results and discussion**

### 295 **3.1 Influence of plasma on jet velocity and turbulence generation**

296 PIV measurements were undertaken to quantify the velocity of the flowing helium gas and the  
297 resulting perturbation of the surrounding quiescent air beyond the jet orifice. **Figure 3** (a-c) shows  
298 the ensemble-averaged two-component velocity vector maps and velocity magnitude ( $U$ )  
299 normalized to the measured exit velocity ( $U_m$ ) for the 0 kV, 10 kV, and 14 kV cases, respectively.  
300 Without a plasma discharge (0 kV case), the undisturbed helium flow appeared laminar over the  
301 entire measurement region, confirmed by the ensemble-averaged centerline velocity ( $U_c$ ) profile in  
302 Figure 3(d). On the application of a 10 kV sinusoidal waveform, a weak discharge was observed to

303 form, indicating gas breakdown had been achieved; under such conditions, little obvious change to  
 304 the velocity profile was observed. An increase in applied voltage from 10 kV to 14 kV led to an  
 305 increase in the length of the visible plasma plume. Comparing Figure 3(b) and 3(c) highlights the  
 306 impact of the applied voltage on the flow structure downstream of the jet orifice, with the higher  
 307 applied voltage resulting in a significant reduction in the length of the laminar flow region. From  
 308 the ensemble-averaged centerline velocity, an abrupt change in gradient is observed at  
 309 approximately  $8 x/D$ , indicating a transition to turbulence. While such results are perhaps the first  
 310 quantitative measurements of velocity within a plasma jet, they are highly consistent with previous  
 311 observations made using qualitative methods such as Schlieren imaging. <sup>[9, 39]</sup>

312



313

314 **Figure 3.** Ensemble averaged particle image velocimetry measurements of the plasma jet obtained  
 315 at applied voltages of (a) 0 kV, (b) 10 kV, and (c) 14 kV, (d) shows the reciprocal of the ensemble-  
 316 averaged centerline velocity ( $U_c$ ) normalized to the measured exit velocity ( $U_m$ ).

317

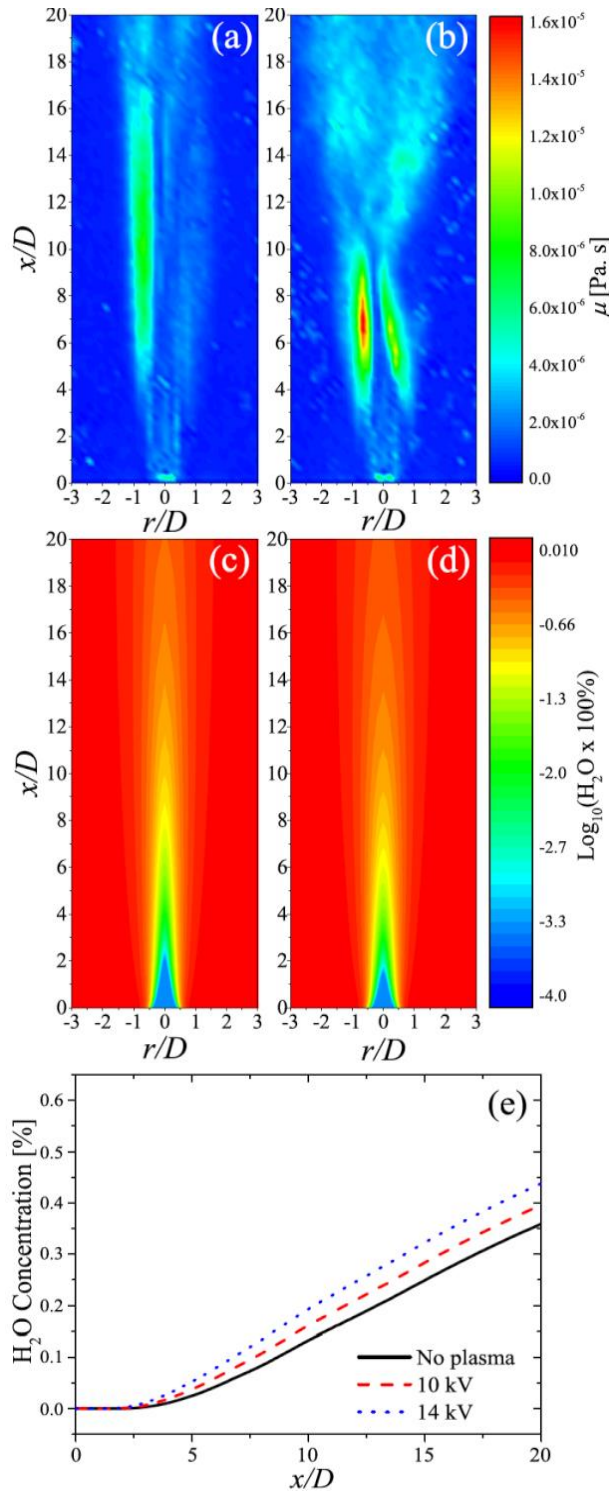
318 In absolute terms, the generation of plasma with an applied voltage of 14 kV was found to increase  
319  $U_m$  by  $0.94 \text{ m s}^{-1}$ , representing a relatively modest increase of approximately 10% compared to the 0  
320 kV case. Such increases in velocity are in line with those predicted by others and are a consequence  
321 of gas heating and electrohydrodynamic forces induced by the plasma, with the latter mechanism  
322 being the most likely dominant factor.<sup>[8, 11]</sup> Notably, the modest change in velocity associated with  
323 plasma generation cannot directly explain the transition to turbulence observed when comparing  
324 Figure 3(a) and 3(c). Past studies on turbulence generation in axisymmetric round jets have revealed  
325 that turbulence initiates due to instabilities within the shear layers at the jet exit that become  
326 amplified as they travel downstream.<sup>[13-17]</sup> As the instabilities grow, they cause velocity fluctuations,  
327 Reynolds shear stresses, and thus the production of turbulence.<sup>[8]</sup> Many previous studies have  
328 explored ‘excited’ jets that employ alternative means to perturb the jet flow in order to investigate  
329 the mechanisms of turbulence generation.<sup>[40-45]</sup> For example, the impact of sonic excitation on the  
330 jet velocity profile shows a remarkable similarity to those observed in this study<sup>[41]</sup>; hence it is  
331 posited that plasma generation is an alternative means to excite an axisymmetric round jet, resulting  
332 in the rapid onset of turbulence through increased shear layer instability with little change to  
333 velocity.

334

335 While the growth of small-scale instabilities within the jet shear layer has a significant impact on  
336 the laminar to turbulent transition, they also provide a mechanism to enhance entrainment of  
337 quiescent air into the laminar region of the plasma jet.<sup>[45]</sup> To investigate the influence of plasma  
338 generation on instabilities in the jet shear layer, the eddy viscosity  $\mu_T$  was calculated. The eddy  
339 viscosity profiles for the two plasma cases investigated in this work are shown in **Figure 4** (a-b).  
340 Three characteristic zones can be observed within the profiles, the first is close to the jet orifice,  
341 where a region of low  $\mu_T$  exists, which can be explained by the fact that this is the laminar region  
342 where the amplitude of velocity fluctuations is small, leading to low turbulent kinetic energy  $k$ , and  
343 consequently, a low  $\mu_T$  as Equation (13) shows. The second zone (e.g.,  $4 - 10 x/D$  in Figure 4(b))



344 coincides with the transition region, as inferred from Figure 3(d), where the value of  $\mu_T$  peaks. This  
345 is attributed to the large scale fluctuations/eddies starting to appear in the transition region, leading  
346 to high turbulent kinetic energy  $k$ , considering that such large fluctuations live long enough to be  
347 transported downstream, the dissipation rate of the turbulent energy  $\varepsilon$  is relatively low in this  
348 region, thus leading to a peak of  $\mu_T$  as follows from Equation (13). The third zone (e.g.  $> 10 x/D$  in  
349 Figure 4(b)) coincides with the turbulent region, as inferred from Figure 3(d), which has a moderate  
350 value of  $\mu_T$ . As known from the energy cascade theory of turbulence,<sup>[46]</sup> the large eddies generated  
351 in the transition region break into smaller eddies in the fully turbulent region, the small eddies are  
352 dissipated into heat due to the physical viscosity of the fluid.<sup>[46]</sup> In this sense, the turbulent kinetic  
353 energy  $k$  is high, while the turbulent dissipation rate  $\varepsilon$  is also high, leading to a moderate value of  $\mu_T$ .  
354 From Figure 4(a-b), it is clear that the eddy viscosity for the 14 kV case has a larger magnitude  
355 compared to the 10 kV case, which is consistent with the PIV results presented in Figure 3(b-c).  
356 When comparing the average value of  $\mu_T$  in zone one ( $x/D < 4$ ) for both cases it is found that  $\mu_T$  for  
357 the 10 kV case is approximately 70%-80% of that for the 14 kV case, indicating that the plasma's  
358 perturbation to the flow in the laminar region is more significant for the 14 kV case in comparison  
359 to the 10 kV case.



360

361

**Figure 4.** Eddy viscosity calculated from PIV measurements for the (a) 10 kV and (b) 14 kV

362

excited plasma jet and the calculated percentage of H<sub>2</sub>O in the helium flow under (c) 0 kV and (d)

363

14 kV conditions; (e) shows the percentage of H<sub>2</sub>O along the jet centerline for all three cases.

364

365

As described in section 2.3, a higher value of the eddy viscosity of  $\mu_T$  indicates a higher value of

366

eddy diffusivity  $D_T$ , which adds to the physical diffusion coefficients, leading to increased

367 entrainment of air into the helium jet for higher values of  $\mu_T$ . To highlight the impact of the plasma-  
368 induced entrainment, Figure 4 (c) and (d) show the computed percentage of H<sub>2</sub>O in the gas mixture  
369 for the 0 kV and 14 kV cases, respectively. Notably, the 0 kV case represents an unperturbed  
370 laminar flow where quiescent air is entrained due to the physical diffusion only. While in the case  
371 of the perturbed flow shown in Figure 4(d), air entrainment occurs due to physical diffusion plus the  
372 “effective” eddy diffusion due to turbulence. The centerline concentration of H<sub>2</sub>O, shown in Figure  
373 4 (e), was set to 0.00004% for all cases, a value obtained from the helium gas provider. Moving  
374 downstream to 2 x/D, the level of H<sub>2</sub>O in the unperturbed 0 kV case was found to increase to be  
375 approximately 0.0005 %. In contrast, the H<sub>2</sub>O concentration in the perturbed case was found to be  
376 0.0034 %, representing a 7-fold increase. Further downstream at 6 x/D, the H<sub>2</sub>O concentration in  
377 the unperturbed case was found to be 0.046%, compared to 0.082% in the perturbed case,  
378 representing a 1.8-fold increase. When moving downstream, the difference between the unperturbed  
379 case and the 14 kV perturbed case diminishes as a result of the increasing density of the gas  
380 mixture, which lowers the value of the eddy diffusivity as defined by Equation (4).

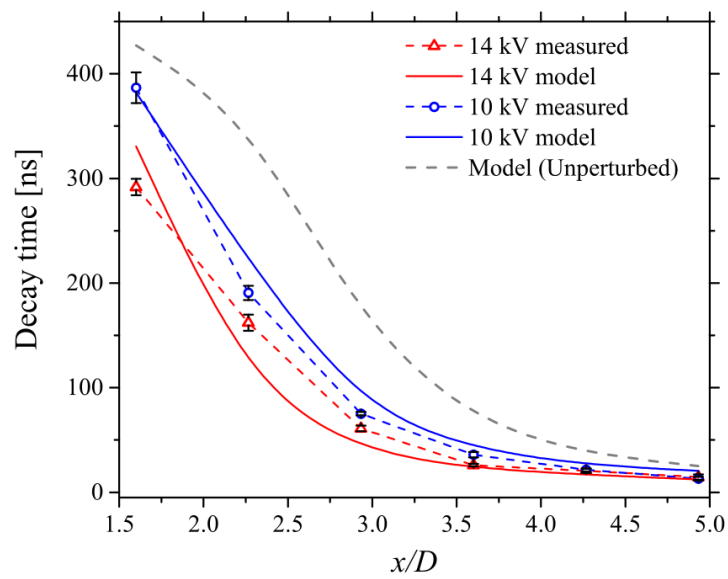
381

### 382 **3.2 OH fluorescence decay rate and absolute density**

383 As described by Yonemori et al. the decay rate of the LIF signal from OH provides a sensitive  
384 indication of the helium-air mixing ratio as the quenching rate of the laser-excited state is strongly  
385 influenced by the density of quenching species present within the flowing helium gas (e.g., N<sub>2</sub>, O<sub>2</sub>,  
386 H<sub>2</sub>O).<sup>[47]</sup> In this study, a comparison between the measured LIF decay rate and computed decay rate  
387 by the model was used to validate the adopted computational approach describing plasma-induced  
388 entrainment, thus enabling the accurate quantification of absolute OH density downstream of the jet  
389 exit. The decay time is obtained from the fitting of the temporal evolution of the LIF signal  
390 intensity, as described in section 2.3. **Figure 5** shows the measured and computed LIF decay time  
391 as a function of downstream spatial position for both the 10 kV and 14 kV cases; additionally, the  
392 predicted decay time for a hypothetical unperturbed (laminar) helium flow is shown. The LIF decay

393 time is shorter at all spatial positions under both 10 and 14 kV excitation compared to what would  
 394 be observed under idealized laminar conditions. As highlighted in Figure 4 (c) and (d), plasma  
 395 generation increases air entrainment, which acts to increase the density of quenchers and thus  
 396 increase the quenching rate of the OH fluorescent state. This result provides experimental evidence  
 397 supporting the hypothesis that plasma generation increases the entrainment of air within the helium  
 398 jet at all spatial positions, not just the fully turbulent region. The calculated decay times closely  
 399 match the measured data points, with both cases showing the agreement.

400



401

402 **Figure 5.** Comparison between measured and calculated decay time of the laser-induced fluorescent  
 403 signal as a function of downstream distance from the jet orifice.

404

405 Using the experimental procedure outlined in section 2.2, the 2D LIF emission profile was compiled  
 406 for both the 10 kV and 14 kV case and is shown in **Figure 6(a)** and **6(b)**, respectively. By  
 407 comparing the centerline LIF intensity obtained from the 2D profile and the computed LIF intensity  
 408 from the collisional radiative model, the absolute ground state OH density was calculated as a  
 409 function of downstream position from the jet exit, shown in Figure 6(c). Consistent with the  
 410 observations made in many previous studies, an increase in applied voltage was observed to  
 411 increase the peak OH density within the plasma plume.<sup>[26]</sup> Given that hydrogen-based species

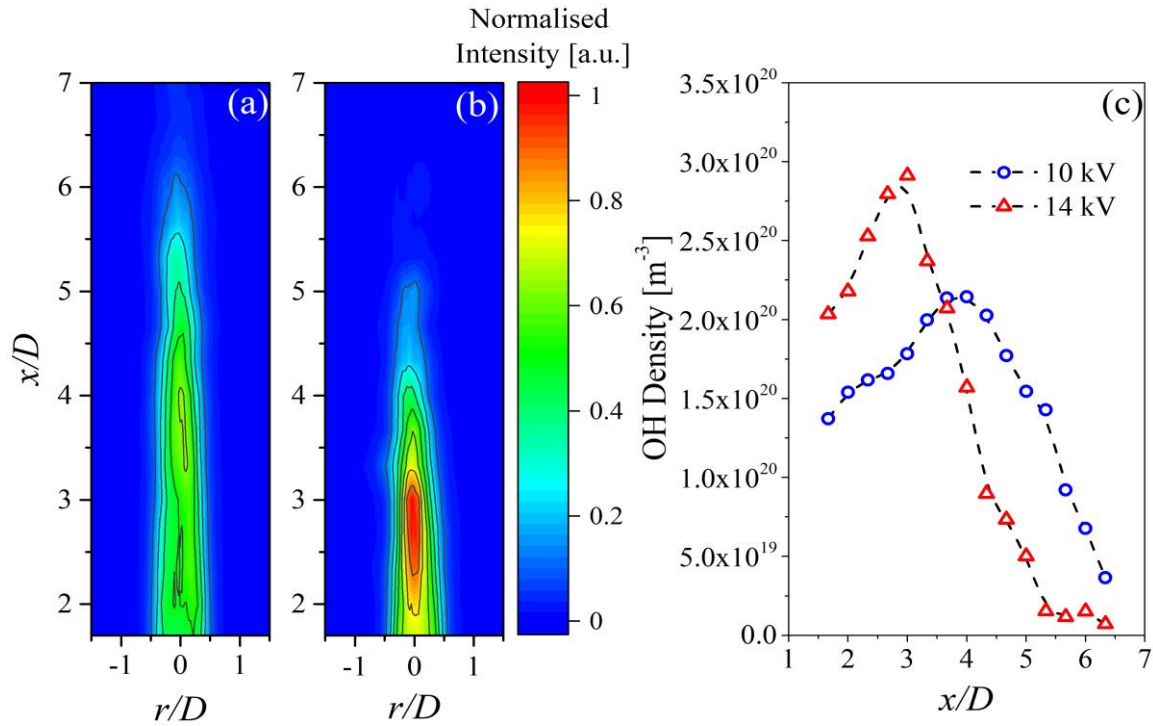
412 densities increase when the air/water vapor fraction increases,<sup>[48]</sup> it becomes likely that an increase  
413 in the applied voltage results in an increase in OH density as a result of not only more intense  
414 discharge conditions but also increased entrainment of air and H<sub>2</sub>O. Critically, the position of peak  
415 OH density was found to vary depending on the applied voltage. This phenomenon is attributed to  
416 the interplay between the physical properties of the plasma (*i.e.*,  $n_e$  and  $T_e$ ) and the fluid dynamics  
417 of the helium jet. With an applied voltage of 14 kV, perturbations within the jet shear layer caused  
418 by plasma generation induce an early transition to a turbulent flow regime, as confirmed in Figure 3  
419 and 4. Under such conditions, the generation of OH close to the jet exit is locally enhanced due to  
420 enhanced H<sub>2</sub>O entrainment combined with the relatively intense discharge conditions. Beyond the  
421 local maxima, the elevated air mole fraction as a result of the enhanced entrainment acts to quench  
422 the discharge and thus impedes OH generation. Conversely, at the lower applied voltage of 10 kV  
423 the discharge is comparatively less intense, meaning less air entrainment and a weaker plasma is  
424 formed, both factors contributing to limit OH production. However, less shear layer perturbation  
425 causes less air entrainment into the helium flow; thus, the discharge can propagate further from the  
426 orifice. Consequently, the concentration of ground-state OH is significantly higher far downstream  
427 from the jet exit in the 10 kV case compared to the 14 kV case.

428

429 The presented findings have considerable implications from a practical perspective as it has been  
430 demonstrated that the density of OH at a given downstream position is strongly influenced by both  
431 the discharge characteristics and its interaction with the quiescent background gas. While it is  
432 generally assumed that a higher plasma generation voltage results in enhanced production of OH,  
433 Figure 6 clearly shows that this only holds true close to the jet orifice. With increasing voltage  
434 comes increasing entrainment, which ultimately begins to quench the discharge and negatively  
435 affects downstream OH production. Counterintuitively, Figure 6(c) indicates that at a position of 5.3  
436  $x/D$  (*i.e.*, 16 mm from the jet exit), there is an order of magnitude more OH from a plasma  
437 generated using 10 kV compared to one generated using 14 kV excitation. These findings

438 demonstrate that the complex interplay between the physicochemical properties of the plasma and  
 439 the fluid dynamic properties of the flowing noble gas must be carefully considered when designing  
 440 plasma jet sources for use in applications such as biomedicine and materials processing.

441



442

443 **Figure 6.** Composite 2D normalized LIF intensity for (a) 10 kV, and (b) 14 kV case. Absolute  
 444 centerline OH density for the 10 kV and 14 kV case as a function of distance from the jet orifice.

445

#### 446 4 Conclusion

447 This contribution has employed Particle Image Velocimetry, Laser-Induced Fluorescence, and  
 448 Computational Fluid Dynamics to explore the interplay between the propagating plasma plume and  
 449 the quiescent background air in an axisymmetric dielectric barrier discharge jet. Despite the rapid  
 450 onset of turbulence observed following plasma ignition, it was demonstrated that the presence of the  
 451 plasma had little impact on the jet exit velocity of the helium flow. Through statistical analysis of  
 452 the measured velocity field from the plasma jet under varying excitation conditions, it was  
 453 determined that plasma generation resulted in shear layer perturbations that grow downstream to  
 454 initiate the early onset of turbulence.

455

456 Using the experimentally derived eddy viscosity, a computational model was developed to calculate  
457 the density of humid air entrained within the helium jet flow. To validate the model, the calculated  
458 decay time of the laser-induced fluorescent state of OH was compared against those measured  
459 experimentally and found to be in good agreement. Finally, the computational model was used to  
460 convert the measured LIF intensity into an absolute OH density from which it was concluded that  
461 OH production is strongly influenced by the interplay between the propagating plasma and the  
462 background air. At high applied voltages, it was found that OH density increases close to the exit  
463 but is rapidly reduced downstream as a result of the elevated air content quenching the discharge.

464

465 In summary, this study demonstrates an intricate link between the physicochemical properties of the  
466 plasma and its interaction with the quiescent air. As many applications rely on the presence of  
467 reactive oxygen and nitrogen species, which are predominantly formed when the plasma interacts  
468 with the background environment, the results of this study provide valuable insight into the  
469 underpinning mechanisms governing these interactions.

470

471 **Acknowledgments:** JLW & MIH would like to acknowledge the support of the Engineering and  
472 Physical Sciences Research Council (Projects EP/S025790/1, EP/S017623/1, EP/R041849/1, and  
473 EP/N021347/1). RDW would like to acknowledge the support of the NATO AVT-254 plasma flow  
474 control group.

475

476 **Keywords:** LIF; PIV; plasma; turbulence.

477 [1] A. J. Knoll, P. Luan, A. Pranda, R. L. Bruce, G. S. Oehrlein, *Plasma Process Polym.* **2018**, *15*,  
478 1700217. doi.org/10.1002/ppap.201700217

479 [2] X. Deng, A. Yu Nikiforov, T. Coenve, P. Cools, G. Aziz, R. Morent, N. De Geyter, C. Leys,  
480 *Sci. Rep.*, **2015**, *5*, 10138. doi.org/10.1038/srep10138

- 481 [3] P. B. Flynn, S. Higginbotham, N. H. Alshraiedeh, S. P. Gorman, W. G. Graham, B. F. Gilmore,  
482 *Int. J. Antimicrob. Agents*, **2015**, *46*, 1. doi.org/10.1016/j.ijantimicag.2015.02.026
- 483 [4] H. Tanaka, M. Mizuno, K. Ishikawa, S. Toyokuni, H. Kajiyama, F. Kikkawa, M. Hori, *Plasma*,  
484 **2018**, *1*, 1. doi.org/10.3390/plasma1010014
- 485 [5] S. Bekeschus, P. Favia, E. Robert, T. Von Woedtke, *Plasma Process Polym.*, **2019**, *16*,  
486 1800033. doi.org/10.1002/ppap.201800033
- 487 [6] S. Iseni, A. Schmidt-Bleker, J. Winter, K-D. Weltmann, S. Reuter, *J. Phys. D. Appl. Phys.*,  
488 **2014**, *47*, 152001. doi.org/10.1088/0022-3727/47/15/152001
- 489 [7] T. Darny, J. M. Pouvesle, J. Fontane, L. Joly, S. Dozias, E. Robert, *Plasma Sources Sci.*  
490 *Technol.*, **2017**, *26*, 105001. doi.org/10.1088/1361-6595/aa8877
- 491 [8] R. D. Whalley, J. L. Walsh, *Sci. Rep.*, **2016**, *6*, 31756. DOI:10.1038/srep31756
- 492 [9] R. Xiong, Q. Xiong, A. Yu Nikiforov, P. Vanraes, C. Leys, *J. Appl. Phys.*, **2012**, *112*, 033305.  
493 DOI:10.1063/1.4746700
- 494 [10] M. Boselli, V. Colombo, E. Ghedini, M. Gherardi, R. Laurita, *Plasma Chem. Plasma Process.*,  
495 **2014**, *34*, 853. DOI:10.1007/s11090-014-9537-1
- 496 [11] S. Park, U. Cvelbar, W. Choe, S. Y. Moon, *Nat. Commun.*, **2018**, *9*, 371. DOI:10.1038/s41467-  
497 017-02766-9
- 498 [12] M. I.Hasan, J. W. Bradley, *J. Phys. D: Appl. Phys.*, **2016**, *49*, 055203. DOI:10.1088/0022-  
499 3727/49/5/055203
- 500 [13] A. Michalke, *Journal of Fluid Mechanics*, **1965**, *23*, 3. DOI:10.1017/S0022112065001520
- 501 [14] M. Lessen, *Nat. Adv. Comm. Aero., Wash.*, **1950**, 979.
- 502 [15] A. Michalke, *J. Fluid Mech.*, **1965**, *23*, 3. DOI:10.1017/S0022112065001520
- 503 [16] A. Michalke, R. Wille, *Proc. 11th Intern. Congr. Appl. Mech.*, **1965**.
- 504 [17] A. Michalke, *Prog. Aerosp. Sci.*, **1972**, *12*, 213. DOI:10.1016/0376-0421(72)90005-X



- 506 [18] A. V. Pipa, T. Bindemann, R. Foest, E. Kindel, J. Röpcke, K-D. Weltmann, *J. Phys. D. Appl.*  
507 *Phys.*, **2008**, *41*, 194011. DOI:10.1088/0022-3727/41/19/194011
- 508 [19] K. McKay, J. S. Oh, J. L. Walsh, J. W. Bradley, *J. Phys. D. Appl. Phys.*, **2013**, *46*, 464018.  
509 DOI:10.1088/0022-3727/46/46/464018
- 510 [20] A. Schmidt-Bleker, J. Winter, S. Iseni, M. Dünnbier, K-D. Weltmann, S. Reuter, *J. Phys. D.*  
511 *Appl. Phys.*, **2014**, *47*, 145201. DOI:10.1088/0022-3727/47/14/145201
- 512 [21] D. Riès, G. Dilecce, E. Robert, P. F. Ambrico, S. Dozias, J. M. Pouvesle, *J. Phys. D. Appl.*  
513 *Phys.*, **2014**, *47*, 275401. DOI:10.1088/0022-3727/47/27/275401
- 514 [22] S. Reuter, J. Winter, A. Schmidt-Bleker, D. Schroeder, H. Lange, N. Knake, V. Schulz-Von  
515 Der Gathen, K. D. Weltmann, *Plasma Sources Sci. Technol.*, **2012**, *21*, 024005. DOI:10.1088/0963-  
516 0252/21/2/024005
- 517 [23] A. Nikiforov, L. Li, N. Britun, R. Snyders, P. Vanraes, C. Leys, *Plasma Sources Sci. Technol.*,  
518 **2014**, *23*, 015015. DOI:10.1088/0963-0252/23/1/015015
- 519 [24] C. Tropea, A. L. Yarin, J. F. Foss, *Springer Handbook of experimental fluid mechanics*,  
520 Springer, NY, USA **2007**.
- 521 [25] L. Li, A. Nikiforov, Q. Xiong, N. Britun, R. Snyders, X. Lu, C. Leys, *Phys. Plasmas*, **2013**, *20*,  
522 093502, DOI: 10.1063/1.4820945),
- 523 [26] S. Yonemori, R. Ono, *J. Phys. D: Appl. Phys.*, **2014**, *47*, 125401, DOI:10.1088/0022-  
524 3727/47/12/125401
- 525 [27] J. Vorac, P. Dvorak, V. Prochaska, J. Ehlbeck, S. Reuter, *Plasma Sources Sci. Technol.*, **2013**,  
526 *22*, 025016, DOI:10.1088/0963-0252/22/2/025016
- 527 [28] T. Verreycken, R. M. Van Der Horst, N. Sadeghi, P. J. Bruggeman, *J. Phys. D. Appl. Phys.*,  
528 **2013**, *46*, 464004. DOI:10.1088/0022-3727/46/46/464004
- 529 [29] G. Dilecce, L. M. Martini, P. Tosi, M. Scotoni, S. De Benedictis, *Plasma Sources Sci.*  
530 *Technol.*, **2015**, *24*, 034007. DOI:10.1088/0963-0252/24/3/034007

531 [30] YF. Yue, XK. Pei, XP. Lu, *IEEE Trans. Radiat. Plasma Med. Sci.*, **2017**, *1*, 6. DOI:  
532 10.1109/TRPMS.2017.2757037

533 [31] R. J. Kee, M. E. Coltrin, P. Glarborg, *Chemically reacting flow: theory and practice*, Wiley-  
534 Interscience, Hoboken, NJ, USA **2003**. DOI:10.1002/0471461296

535 [32] R. B. Bird, W. E. Stewart, E. N. Lightfoot, *Transport Phenomena*, 2nd edition, John Wiley &  
536 Sons, NY, USA **2002**.

537 [33] S. P. Wasik, K. E. McCulloh, *J. Res. Natl. Bur. Stand.*, **1968**, *73A*, 2.

538 [34] J. Rohling, J. Shen, C. Wang, J. Zhou, C. E. Gu, *Appl. Phys. B*, **2007**, *87*, 355.  
539 DOI:10.1007/s00340-007-2595-9

540 [35] C. V. Paganelli, F. K. Kurata, *Respiration Physiology*, **1977**, *30*, 15. DOI:10.1016/0034-  
541 5687(77)90018-4

542 [36] T. J. Chung, *Computational fluid dynamics*, Cambridge University Press, Cambridge, UK  
543 **2002**.

544 [37] D. Xu, J. Chen, *Exp. Therm. Fluid Sci.*, **2013**, *44* 662.  
545 DOI:10.1016/j.expthermflusci.2012.09.006

546 [38] C. Gualtieri, A. Angeloudis, F. Bombardelli, S. Jha, T. Stoesser, *Fluids*, **2017**, *2*, 17.  
547 DOI:10.3390/fluids2020017

548 [39] M. Boselli, V. Colombo, M. Gherardi, R. Laurita, A. Liguori, P. Sanibondi, E. Simoncelli, A.  
549 Stancampiano, *IEEE Trans. Plasma Sci.*, **2015**, *43*, 3. DOI: 10.1109/TPS.2014.2381854

550 [40] H. Sato, *J. Phys. Soc. Jpn.*, **1956**, *11*, 702. DOI:10.1143/JPSJ.11.702

551 [41] H. Sato, *J. Phys. Soc. Jpn.*, **1959**, *14*, 1797. DOI:10.1143/JPSJ.14.1797

552 [42] E. Gutmark, C-M. Ho, *Phys. Fluids*, **1983**, *26*, 2932. DOI:10.1063/1.864058

553 [43] J. Cohen, I. Wygnanski, *J. Fluid Mech.*, **1987**, *176*, 191. DOI:10.1017/S0022112087000624

554 [44] S. W. Rienstra, *J. Sound Vib.*, **1983**, *86*, 4. DOI:10.1016/0022-460X(83)91019-2

555 [45] J. Westerweel, C. Fukushima, J.M. Pederson, J. C. R. Hunt, *Phys. Rev. Lett.*, **2005**, *95*,  
556 174501. DOI:10.1103/PhysRevLett.95.174501

- 557 [46] B. Lautrup, *Physics of continuous matter: exotic and everyday phenomena in the macroscopic*  
558 *world*, Institute of Physics, Bristol, UK **2005**.
- 559 [47] S. Yonemori, Y. Nakagawa, R. Ono, T. Oda, *J. Phys. D. Appl. Phys.*, **2012**, *45*, 225202.  
560 DOI:10.1088/0022-3727/45/22/225202
- 561 [48] T. Murakami, K. Niemi, T. Gans, D. O'Connell, W. G. Graham, *Plasma Sources Sci. Technol.*,  
562 **2013**, *22*, 015003. DOI:10.1088/0963-0252/22/1/015003
- 563